Journal of Materials Chemistry

Cite this: J. Mater. Chem., 2011, 21, 8887

www.rsc.org/materials

PAPER

Ternary PtSnRh–SnO_2 nanoclusters: synthesis and electroactivity for ethanol oxidation fuel cell reaction†

Wenxin Du,[a] Qi Wang,[b] Carlo A. LaScala,[a] Lihua Zhang,[c] Dong Su,[c] Anatoly I. Frenkel,[d] Virendra K. Mathur[a] and Xiaowei Teng*[a]

Received 13th December 2010, Accepted 11th April 2011
DOI: 10.1039/c0jm04358c

Carbon supported ternary $Pt_{52}Sn_{(36-x)}Rh_{12}$–$Sn_xO_{2x}$ electrocatalysts with the average diameter of 2.8 ± 0.5 nm were synthesized using a Polyol process followed by thermal treatment. Several techniques including high resolution transmission electron microscopy (HRTEM), X-ray diffraction (XRD) and extended X-ray absorption fine structure (EXAFS) were used to identify the coexistence of homogeneously distributed Pt/Sn/Rh random alloy and non-alloyed SnO_2 throughout the catalyst. The $Pt_{52}Sn_{(36-x)}Rh_{12}$–$Sn_xO_{2x}$ catalyst showed a superior long-term activity and stability towards ethanol oxidation than the commercial Pt catalyst. Our data of ternary Pt/Sn/Rh catalysts with different chemical compositions and crystalline structures also indicated that the superior performance of $Pt_{52}Sn_{(36-x)}Rh_{12}$–$Sn_xO_{2x}$ might result from the electronic effect of the Pt/Sn/Rh random alloy.

Introduction

There has been a growing interest in electrocatalytic conversion of small organic molecules (SOMs) into electrical energy by the low temperature direct fuel cell reaction. Ethanol becomes an attractive fuel in the fuel cell reactions compared with methanol and hydrogen, because it is less toxic, available from renewable resources, and ease of storage and transport. Moreover, due to the nature of twelve-electron transfer upon complete oxidation, ethanol has a higher energy density (7 kW h L^{-1} for ethanol, 5 kW h L^{-1} for methanol and 3 kW h L^{-1} for hydrogen compressed at 5000 psi).[1–4] A major impediment to the commercialization of ethanol fuel cell stacks is the difficulty in designing an effective electrocatalyst having a high tolerance for the strongly adsorbed species coming from the dissociative adsorption of ethanol.[1,5–8] Recent efforts to develop electrocatalysts for ethanol oxidation have been concentrated on the ternary systems containing Pt, Rh and Sn.[9–14] Although mechanistic details remain obscure, the prevailing view indicates that Rh increases the yield of CO_2 by helping break the C–C bond, while Sn supplies the oxygenated species needed to oxidize the blocking intermediates.[6,14,15] Thus, formation of an alloyed structure where Pt, Rh and Sn atoms are in close proximity could be favorable because the cooperative effect from Rh and Sn in the vicinity of Pt sites could provide high activity toward ethanol oxidation and better tolerance for poisoning species. The synthesis of Pt/Rh/Sn catalysts *via* an under potential deposition (UPD) method, as well as the electrocatalytic and *in situ* spectroscopic measurements for ethanol oxidation first reported by Adzic and co-workers, is quite encouraging.[11] However the Pt/Rh/Sn ternary alloy structures in these systems are difficult to assess, and the UPD method may not be easy for the mass production of electrocatalysts. In this context, a controlled bulk synthetic procedure which is easy to scale-up, as well as the synthesis of Pt/Rh/Sn ternary homogeneous alloy catalysts, will optimize the activity of Pt/Rh/Sn towards ethanol oxidation reaction.

In addition to the lack of synthetic procedures of Pt/Sn/Rh ternary alloy nanoparticles, the structural characterization of Pt/Sn/Rh is not trivial, partially reflecting the complexity of heterogeneous nature imposed by the ternary nanoscale system. Extended X-ray absorption fine structure (EXAFS) is a well established tool for investigating the element-resolved structure of the nanomaterials, since the local environment and electronic properties of atoms of each resonant element can be studied separately. Although EXAFS has been widely used to characterize heterogeneous structure of binary system, the characterization of ternary metallic alloy nanostructures *via* EXAFS has not been reported.

Here we report the synthesis of carbon supported Pt/Sn/Rh–SnO_2 nanoclusters *via* a facile wet chemistry synthesis. Extended X-ray absorption fine structure (EXAFS), for the first time, has

[a]*Department of Chemical Engineering, University of New Hampshire, Durham, NH, 03824, USA. E-mail: xw.teng@unh.edu; Fax: +1 603 862 3747; Tel: +1 603 862 4245*
[b]*Department of Chemical Engineering, University of Delaware, Newark, DE, USA 19716*
[c]*Center for Functional Nanomaterials, Brookhaven National Laboratory, Upton, NY, USA 11973*
[d]*Department of Physics, Yeshiva University, New York, NY, USA 10016*

† Electronic supplementary information (ESI) available: EDS (Fig. S1), XRD (Fig. S2), EXAFS spectra and fitting results (Fig. S3 and S4), CV, IT curves and results of all the catalysts (Fig. S5 and S6), and TEM images of $Pt_{36}Rh_{10}$–$Sn_{54}O_{108}$/C and $Pt_{30}Rh_{30}$–$Sn_{40}O_{80}$/C (Fig. S7). See DOI: 10.1039/c0jm04358c

identified the coexistence of Pt/Sn/Rh homogeneous ternary alloy and a non-alloyed tin oxide inside the nanocatalyst. The unique Pt/Sn/Rh–SnO_2 heterogeneous structures between Pt, Sn and Rh showed the advantages of high activity and stability during ethanol oxidation.

Experimental

Material synthesis

In a typical synthetic procedure of $Pt_{52}Rh_{12}Sn_{36}$ nanostructures, 8 mL ethylene glycol (AR, Mallinckrodt Chemicals) and 55 mg PVP ($M_w = 58\,000$, Acros) were pre-mixed in a 50 mL three-neck flask, and followed with heating up to 170 °C using oil bath under argon protection. Then a fresh-made precursor mixture of Na_2PtCl_4 (29.4 mg, 0.064 mmol, Alfa Aesar, 99.95%), K_3RhCl_6 (7.1 mg, 0.016 mmol, Alfa Aesar, 99.99%), and $SnCl_2$ (6.1 mg, 0.032 mmol, Alfa Aesar, 99%), which was dissolved in 3 mL ethylene glycol by sonication, was injected into the pre-heated flask. The solution was maintained at 170 °C for 30 min before cooling down to room temperature. The product was washed and precipitated out once by mixing 10 mL of acetone with 3 mL of the product, followed by centrifuging at 4500 rpm for 5 min. Then the precipitate was re-dispersed in 12 mL of ethanol plus 6 mL of de-ionized water. The synthesis of other Pt/Rh/Sn nanostructures with different stoichiometries as well as $Pt_{44}Rh_{56}$ NPs followed the same procedure except for the adjustment of precursor amount added in. The $Pt_{55}Sn_{45}$ NPs were prepared following reported procedures with adjustment. The re-dispersed Pt/Rh/Sn nanostructures were mixed with 90 mg of activated carbon (Vulcan, XC-72R) for 16 h at a 700 rpm stirring rate. The carbon supported product was precipitated out by adding an appropriate amount of acetone before drying under argon flow. The dried sample was then thermally treated at 300 °C for 1 hour in air, followed by 50 °C for 20 min in H_2.

TEM, EDS and XRD

The regular TEM images were taken on a Zeiss/LEO 922 Omega TEM which was operated at 200 kV. Data analysis was performed on ImageJ software. HR-TEM was performed using a field-emission JEM 2100FEG. Image acquisition and analysis was performed using Gatan Digital Micrograph. Energy dispersive X-ray spectroscopy (EDS) was carried out on Amray 3300FE field emission SEM with PGT Imix-PC microanalysis system. At least 5 different points were collected to acquire reliable chemical composition for each sample. X-Ray diffraction (XRD) patterns were recorded by the Bruker AXS instrument equipped with a GADDS (General Area Detector Diffraction System) detector. A Cu Kα X-ray tube was employed as an X-ray source.

Extended X-ray absorption fine structure (EXAFS)

EXAFS experiments were performed at beam lines X18B and X19A at the National Synchrotron Light Source, Brookhaven National Laboratory, Upton, New York. The storage ring energy was 2.5 GeV, and the ring current was in the range of 110–300 mA. A double-crystal Si (111) monochromator was used to scan X-ray energy from −150 eV to 1700 eV relative to the Pt L_3 edge (11 564 eV), while −150 eV to ~1200 eV relative to the Rh K edge (23 220 eV) and Sn K edge (29 200 eV). Each carbon supported sample (~100 mg) was brushed onto the tape. The tape was folded several times for adequate uniformity and thickness for transmission XAFS measurement. Metal foils (Pt, Rh and Sn) were measured in reference modes for X-ray energy calibration and data alignment. EXAFS data processing and analysis were performed using the IFEFFIT package. Several parameters describing electronic properties (*e.g.*, correction to the photoelectron energy origin) and local structural environment (coordination number (N), bond length (R) and mean squared disorder parameter (σ^2)) around absorbing atoms were varied in the fit. For evaluation purpose, Pt–metal (N_{Pt-M}), Rh–metal (N_{Rh-M}), and Sn–metal (N_{Sn-M}) coordination numbers were defined as:

$$N_{Pt-M} = N_{Pt-Pt} + N_{Pt-Sn} + N_{Pt-Rh}$$

$$N_{Rh-M} = N_{Rh-Pt} + N_{Rh-Sn} + N_{Rh-Rh}$$

$$N_{Sn-M} = N_{Sn-Pt} + N_{Sn-Sn} + N_{Sn-Rh}$$

Electrochemical measurements

The electrochemical properties of as-made catalysts were evaluated with a CHI 660 single channel electrochemical workstation (CH instruments, Inc.). A three-electrode system, including a glassy carbon working electrode, a platinum wire counter electrode and a Ag/AgCl (1 M KCl) reference electrode, was employed for the test. The home made carbon supported catalysts as well as the commercial catalyst Pt/C (ETEK, 20 wt% of Pt) were dispersed in de-ionized water and sonicated well before drop-casting on the working electrode. Typically 10 μL of catalyst inks which contained 2–3 μg of metal was loaded to get comparable results. After being dried in the fume hood, another 10 μL of Nafion solution (0.5%, VNafion/Vwater) was drop-cast on top of the catalyst layer and dried for 30 min to ensure the catalyst tightly sticks on the glassy carbon surface. The cyclic voltammetry (CV) was performed in an Ar-purged 0.5 M sulfuric acid (99.999%, Sigma-Aldrich) solution recording from −0.27 V to 0.35 V to collect H adsorption/desorption information for the evaluation of electrochemical surface area (ECSA). One Pt (or Rh) active site was assumed only to interact with one hydrogen atom and 210 μC cm^{-2} of charge for the monolayer of H adsorption/desorption was used in ECSA calculation for all PtRhSn/C and Pt/C catalysts. CVs were also conducted for those as-made catalysts in an Ar-protected 0.5 M H_2SO_4/0.5 M ethanol solution recording from −0.1 V to 0.35 V to determine their catalytic activity towards ethanol oxidation. The potential sweeping rate was kept at 30 mV s^{-1} for all the CV measurements. Chronoamperometry measurement (IT) was carried out at a potential of 0.25 V for 20 hours right after the completion of CV to get long term performance of each catalyst. All the electrochemical measurements were performed at ambient room temperature.

Result and discussion

The catalysts were synthesized through the Polyol process followed by a thermal treatment at 300 °C in the open air. The original Pt/Sn/Rh appears as short nanowires with an average width of 2.2 ± 0.4 nm and varied lengths (Fig. 1a). After deposition on the carbon support and following thermal treatment, Pt/Sn/Rh appeared as a series of nanoparticles with an average diameter of 2.8 ± 0.5 nm (Fig. 1b) that were distributed evenly on the carbon support. We notice that after thermal treatment at 300 °C in air, the morphology of Pt/Sn/Rh changed from the original short nanowire to nearly spherical nanoparticles. The shape transformation might be attributed to the lower melting points of Pt/Sn/Rh nanowires than that of bulk materials due to the changes of surface tension in the nanoscale. Similar phenomena have been also reported in Pt, Au nanoparticles and Au nanorods.[16–18] The chemical composition was determined as $Pt_{52}Rh_{12}Sn_{36}$ by energy dispersive X-ray spectroscopy (EDS) (Fig. S1†). The HR-TEM image in Fig. 1c shows that the carbon-supported catalysts have good crystalline structure with well-defined fringes. The distances between the adjacent fringes were estimated to be 0.24 nm, 0.21 nm and 0.34 nm, which can be attributed to the (111) and (200) planes of cubic Pt alloy, as well as the (110) plane of tetragonal SnO_2, respectively.

The X-ray diffraction (XRD) patterns of carbon supported $Pt_{52}Rh_{12}Sn_{36}$ catalyst showed a broad face-centered cubic (FCC) structure, but no SnO_2 peaks were seen (Fig. S2†). All diffraction peaks for $Pt_{52}Rh_{12}Sn_{36}$/C shifted to higher two-theta angles compared with Pt/C, further confirming the formation of a Pt-containing alloy. However, the opposing effects on lattice contraction/expansion from Rh- or Sn-alloyed Pt, as well as the peak broadening due to small size of the catalyst, made it difficult to identify the formation of any binary or ternary alloy between Pt, Sn and Rh solely from HR-TEM and XRD data. To further determine the existence of any binary or ternary alloy, the catalyst was analyzed by EXAFS with the information input from TEM, XRD and EDS.

The Fourier transform magnitudes of EXAFS data and theoretical fits for Pt, Sn and Rh are shown in Fig. S3 and S4†.

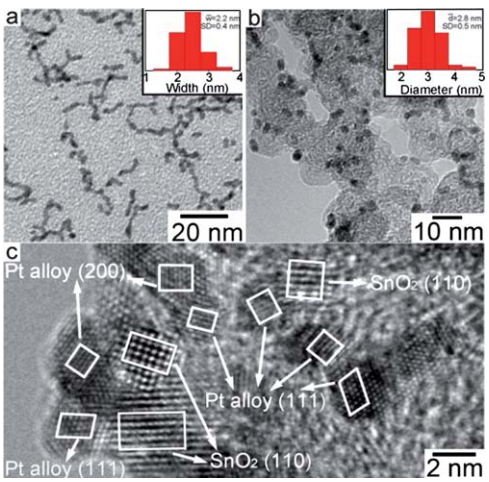

Fig. 1 TEM images of (a) as-made unsupported $t_{52}Rh_{12}Sn_{36}$ and (b and c) carbon-supported $Pt_{52}Rh_{12}Sn_{36}$ catalyst after thermal treatment.

The best fit values of coordination numbers and bond distances are summarized in Table 1. Evident from Table 1, heterogeneous bonds were formed between Rh–Sn, Pt–Sn as well as Pt–Rh. In all three cases, the bond distances showed much more similarity to those of the Pt–Pt and Rh–Rh bonds in the FCC structure than the Sn–Sn bond in the tetragonal structure, strongly supporting the proposition of Pt/Sn/Rh ternary alloy in the FCC-like structure. The presence of metallic Sn was demonstrated well in the R-space XAFS plot of such sample in comparison to that of SnO_2 (Fig. S3i†). However, the coordination numbers of Rh–Rh (N_{Rh-Rh}) and Sn–Sn (N_{Sn-Sn}) were not identified, even though distinct Sn–Pt coordination was observed ($N_{Sn-Pt} = 5.4 \pm 2.3$). This might be due to the low concentration of metallic Rh and Sn, evident also by the less distinct Sn–Rh coordination number ($N_{Sn-Rh} = 1.0 \pm 0.6$). On the other hand, the strong Sn–O coordination ($N_{Sn-O} = 2.9 \pm 0.7$) unambiguously indicated the formation of tin oxide clusters, confirmed also by the results obtained independently from HR-TEM. Meanwhile, whether Rh is also present as an oxide is unclear due to the high uncertainty of the Rh–O coordination ($N_{Rh-O} = 2.5 \pm 2.8$).

By analyzing the metal–metal total coordination number, the metal placement pattern within the $Pt_{52}Rh_{12}Sn_{36}$/C catalyst is examined. Since Rh and Sn can be present in both oxides and metallic (alloy) phases, the values of Rh–metal coordination number ($N_{Rh-M} = 6.6 \pm 1.3$) and Sn–metal coordination number ($N_{Sn-M} = 6.4 \pm 2.4$) have meanings of average results over the alloy and oxide phases. If these values are compared with the Pt–M coordination numbers directly, such comparison will result in underestimating the distribution of Rh–M and Sn–M in the alloy phase. Had XAFS been able to extract these numbers for the metal alloy phase separately, they would have been higher and thus closer to the Pt–metal coordination number ($N_{Pt-M} = 8.5 \pm 0.4$), indicating a more homogeneous alloy than the average coordination numbers indicate (see Experimental section for more details about EXAFS analysis).[19–21] Therefore, we suggest the coexistence of bi-phase throughout the $Pt_{52}Rh_{12}Sn_{36}$/C catalyst: a homogeneous alloy containing Pt, Sn and Rh, and tetragonal SnO_2 clusters in a segregated phase. Combined with overall chemical composition obtained from EDS and fitting results from EXAFS, we attribute the overall composition of $Pt_{52}Rh_{12}Sn_{36}$ as $Pt_{52}Sn_{(36-x)}Rh_{12}$–$Sn_xO_{2x}$/C. In this context, the total Sn molar ratio is 36%, of which X% of Sn species existed as SnO_2, and $(36 - X)$% of Sn species existed as metallic Sn alloying with Pt and Rh.

The cyclic voltammograms (CVs) of the $Pt_{52}Sn_{(36-x)}Rh_{12}$–$Sn_xO_{2x}$/C catalyst in acid solution are shown in Fig. 2a. During the sweeping between −0.27 and 0.8 V (*vs.* Ag/AgCl), the reduction peaks of metals in the cathodic waves (between 0.35 V and 0.45 V) shifted to higher potentials continuously. The steady-state Pt-like CV was reached after 40 cycles sweeping, indicating significant dissolution of Rh and Sn in the surface composition. In order to prevent Rh and Sn from leaching, the electrochemical surface areas (ECSAs) of the catalysts were measured by potential cycling between −0.27 and 0.35 V (Fig. 2b).[22]

Fig. 2c shows the polarization curves of the catalysts in an ethanol-containing electrolyte. $Pt_{52}Sn_{(36-x)}Rh_{12}$–$Sn_xO_{2x}$/C exhibited a mass current density of 157.1 mA mg^{-1} (Pt + Rh) on the basis of the total mass of Pt and Rh at 0.35 V, which was

Table 1 XAFS analysis results for $Pt_{52}Sn_{(36-x)}Rh_{12}$–$Sn_xO_{2x}$/C, $Pt_{36}Rh_{10}$–$Sn_{54}O_{108}$/C and $Pt_{30}Rh_{30}$–$Sn_{40}O_{80}$/C

Samples	$Pt_{52}Sn_{(36-x)}Rh_{12}$–$Sn_xO_{2x}$/C	$Pt_{36}Rh_{10}$–$Sn_{54}O_{108}$/C	$Pt_{30}Rh_{30}$–$Sn_{40}O_{80}$/C
N_{Pt-Pt}	7.0 ± 0.2	6.3 ± 0.2	4.8 ± 0.3
N_{Pt-Sn}	0.4 ± 0.3		
N_{Pt-Rh}	*1.1 ± 0.2*[a]	*1.5 ± 0.2*[a]	*3.2 ± 0.3*[a]
$\boldsymbol{N_{Pt-M}}$	**8.5 ± 0.4**	**7.8 ± 0.3**	**8.0 ± 0.4**
N_{Rh-Rh}		1.1 ± 0.7	1.5 ± 0.7
N_{Rh-O}	2.5 ± 2.8	0.9 ± 0.8	1.6 ± 0.6
N_{Rh-Pt}	4.7 ± 0.8	5.3 ± 0.7	3.2 ± 0.3
N_{Rh-Sn}	1.9 ± 1.0		1.4 ± 1.2
$\boldsymbol{N_{Rh-M}}$[b]	**6.6 ± 1.3**	**6.4 ± 1.0**	**6.1 ± 2.2**
N_{Sn-Sn}[b]		2.1 ± 0.2	1.7 ± 0.2
N_{Sn-O}[c]	2.9 ± 0.7	6.4 ± 0.5	5.0 ± 0.5
N_{Sn-Pt}	5.4 ± 2.3		
N_{Sn-Rh}	1.0 ± 0.6		*1.0 ± 0.9*[a]
$\boldsymbol{N_{Sn-M}}$[d]	**6.4 ± 2.4**	**0**	**1.0 ± 0.9**
R_{Pt-Pt}/Å	2.755 ± 0.001	2.745 ± 0.002	2.742 ± 0.003
R_{Pt-Rh}/Å	2.746 ± 0.005	2.737 ± 0.006	2.733 ± 0.004
R_{Pt-Sn}/Å	2.758 ± 0.015		
R_{Rh-Rh}/Å		2.720 ± 0.013	2.719 ± 0.008
R_{Rh-O}/Å	2.033 ± 0.030	1.993 ± 0.030	2.020 ± 0.015
R_{Rh-Pt}/Å	2.746 ± 0.005	2.737 ± 0.006	2.733 ± 0.004
R_{Rh-Sn}/Å	2.683 ± 0.012		2.771 ± 0.032
R_{Sn-Sn}/Å		3.209 ± 0.017	3.212 ± 0.015
R_{Sn-O}/Å	2.046 ± 0.011	2.050 ± 0.008	2.052 ± 0.007
R_{Sn-Pt}/Å	2.758 ± 0.015		
R_{Sn-Rh}/Å	2.683 ± 0.012		2.771 ± 0.032

[a] Coordination numbers in italics were calculated based on the atomic ratio (X) obtained from EDS: $N_{Pt-Rh} = N_{Rh-Pt} \cdot X_{Rh}/X_{Pt}$, $N_{Sn-Rh} = N_{Rh-Sn} \cdot X_{Rh}/X_{Sn}$. [b] Coordinations of metallic Sn–Sn (for Pt/Sn/Rh alloys) and oxidized Sn–Sn (for SnO_2) were fitted separately. [c] In the fitting of SnO_2 in the $Pt_{36}Rh_{10}$–$Sn_{54}O_{108}$/C and $Pt_{30}Rh_{30}$–$Sn_{40}O_{80}$/C, $N_{Sn-Sn} : N_{Sn-O}$ was set to 1 : 3. [d] N_{Sn-Sn} in oxide structure was excluded in the calculation of N_{Sn-M}.

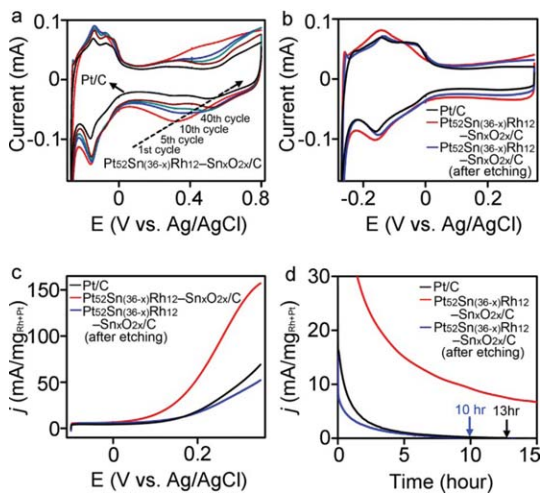

Fig. 2 Electrochemical measurements of the carbon-supported $Pt_{52}Sn_{(36-x)}Rh_{12}$–$Sn_xO_{2x}$ and Pt (ETEK) catalysts. (a) CVs in acid only electrolyte sweeping from −0.27 V to 0.8 V, (b) CVs in acid only electrolyte sweeping from −0.27 V to 0.35 V, (c) CVs in ethanol/acid electrolyte sweeping from −0.1 V to 0.35 V, and (d) IT measurements at 0.25 V in ethanol/acid electrolyte.

2.3 times greater than that of commercial Pt/C (ETEK). Fig. 2d further shows chronoamperometry (IT) measurements conducted at 0.25 V. Our catalyst exhibited a superior long-term activity with the mass current density of 6.7 mA mg^{-1} (Rh + Pt) after 15 hours reaction, while Pt/C showed no activity after 13 hours. A synergic effect between Pt, Sn and Rh can be further seen from $Pt_{52}Sn_{(36-x)}Rh_{12}$–$Sn_xO_{2x}$/C sample after etching off Rh and Sn by intensive sweeping between −0.27 V and 0.8 V as shown in Fig. 2a, where much reduced activities were observed. Moreover, PtSnOx/C and PtRh/C binary catalysts made by a similar method also showed lower activity than the ternary catalyst, also confirming the cooperative effect of Pt, Sn and Rh towards ethanol oxidation (Table 2).

Voltammetry was used to determine the surface area of the catalysts by measuring H adsorption before and after 20 hours of chronoamperometry measurements as shown in Fig. 3. Integrating the charges between −0.22 V and 0.11 V associated with H adsorption shows about 22% loss of initial ECSA. However, for Pt/C, ~40% of the initial ECSA was lost after the reaction. The much preserved ECSA in $Pt_{52}Sn_{(36-x)}Rh_{12}$–$Sn_xO_{2x}$/C might be attributed to the improved stability acquired from interfacial structures between Pt/Sn/Rh and tin oxide,[14] as well as the close proximity of Sn with Pt and Rh atoms throughout the Pt/Sn/Rh random alloy, which mitigated Pt and Rh sites from being poisoned by adsorbed intermediates such as CO or CHx species.[23,24]

Carbon supported Pt/Sn/Rh catalysts with different chemical compositions were also synthesized and tested for ethanol oxidation as summarized in Table 2 (see Fig. S5 and S6 for CVs and ITs, and Fig. S7† for TEM images). $Pt_{36}Rh_{10}Sn_{54}$/C and $Pt_{30}Rh_{30}Sn_{40}$/C showed less mass current density and specific current density (averaged by ECSA) than $Pt_{52}Sn_{(36-x)}Rh_{12}$–$Sn_xO_{2x}$/C, but equivalent or superior activities as compared to commercial Pt/C, especially in IT measurements. EXAFS data showed that Sn existed mainly as tin oxide in $Pt_{36}Rh_{10}Sn_{54}$/C and $Pt_{30}Rh_{30}Sn_{40}$/C catalysts, evident from the correlated Sn–Sn and Sn–O bonds as well as the less distinct Pt–Sn and Rh–Sn coordinations (Table 1). Together with the observation of stronger

Table 2 CV and IT results of supported Pt/Rh/Sn catalysts with different chemical compositions

Catalysts	j^a/μA cm^{-2}		j^b/mA mg^{-1}		Particle size^e/nm
	CV^c	IT^c	CV^c	IT^c	
$Pt_{52}Sn_{(36-x)}Rh_{12}$–$Sn_xO_{2x}$/C	303.6	12.9	157.1	6.7	2.6
$Pt_{36}Rh_{10}$–$Sn_{54}O_{108}$/C	203.8	11.3	85.2	4.8	2.6
$Pt_{30}Rh_{30}$–$Sn_{40}O_{80}$/C	106.6	3.6	48.5	1.6	2.5
Pt/C (ETEK)	126.2	<0	69.0	<0	2.7
$Pt_{52}Sn_{(36-x)}Rh_{12}$–$Sn_xO_{2x}$/C after etching	91.9	<0	52.2	<0	N/A
$Pt_{55}Sn_{45}O_x$/C	N/A^d	N/A^d	21.5	1.6	3.5
$Pt_{44}Rh_{56}$/C	43.0	<0	5.2	<0	4.0

^{a} Specific current density was averaged by the ECSA. ^{b} Mass current density was averaged by the total mass of Rh and Pt. ^{c} CVs were collected at 0.35 V, ITs were collected at 0.25 V after 15 hours reaction. ^{d} ECSA cannot be calculated due to the less feature in hydrogen adsorption region. ^{e} Calculated from Pt alloy plane (111) in XRD.

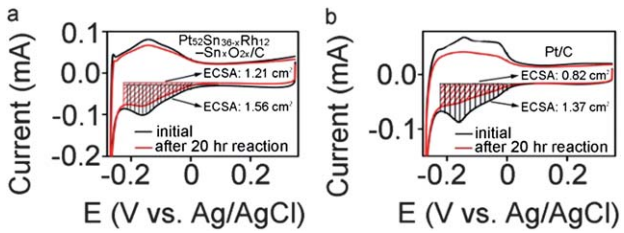

Fig. 3 ECSAs of (a) $Pt_{52}Sn_{(36-x)}Rh_{12}$–$Sn_xO_{2x}$/C and (b) Pt/C (ETEK) before and after 20 hours of reaction in ethanol-containing electrolyte.

Pt–Rh heterogeneous interaction, one may conclude that $Pt_{36}Rh_{10}Sn_{54}$/C and $Pt_{30}Rh_{30}Sn_{40}$/C formed a bi-phase structure of Pt/Rh binary alloy with segregated SnO_2 clusters, in sharp contrast to the bi-phase containing ternary alloy and SnO_2 found in $Pt_{52}Rh_{12}Sn_{36}$/C.

The background corrected and normalized X-ray absorption near-edge structure (XANES) spectra of those three nano-catalysts are presented in Fig. 4. $Pt_{36}Rh_{10}$–$Sn_{54}O_{108}$/C and $Pt_{30}Rh_{30}$–$Sn_{40}O_{80}$/C have almost identical Sn K edge profiles (Fig. 4a and b), featuring the characteristic white line (the intense peak at the absorption edge) of SnO_2 particles (~40 nm in diameter).[21] In contrast, the white line intensity of $Pt_{52}Sn_{(36-x)}Rh_{12}$–$Sn_xO_{2x}$/C is higher than that of metallic Sn and lower than that of SnO_2 particles. Moreover, its white line position (29 206.4 eV) also exhibits the value between bulk metallic Sn (29 203.1 eV) and SnO_2 particles (29 208.3 eV). All these results point out Sn was not completely oxidized in $Pt_{52}Sn_{(36-x)}Rh_{12}$–$Sn_xO_{2x}$/C. A mixture of a SnO_2 phase and a metallic Sn phase is a likely explanation of the XANES profile,[25] supporting the proposed ternary Pt/Sn/Rh alloy–tin oxide heterogeneous structure identified independently from XAFS analysis. Fig. 4c and d show that the intensity of the Pt white line feature in the L_3 edge from $Pt_{52}Sn_{(36-x)}Rh_{12}$–$Sn_xO_{2x}$/C is considerably lower than those of the other two samples, as well as the bulk Pt (foil). Since the white line features in the Pt L_3 edge arise from 2p to 5d dipole transitions, these observations point to a more filled d band, as well as a lower lying d band center at the Pt site. The modified d band feature may result from the alloy effect of Sn, which has been observed in the PtSn catalyst.[25] Since the white line features in the Rh K edge represent the transition from 1s orbital to hybridized 5p and 4d orbitals, the down shifted white line observed in $Pt_{52}Sn_{(36-x)}Rh_{12}$–$Sn_xO_{2x}$/C may suggest a more filled d band of Rh in the sample as shown in Fig. 4e and f.[26]

It is known that in the oxidation of SOMs in the direct fuel cell reaction, high activity of a binary or ternary catalyst is attributed not only to the bi-functional effect (as Pt atoms provide active sites, transition metals provide oxygenated species to oxidize the intermediates) but also to the electronic structure modified by binary or ternary alloy formation.[6,27–36] The superior activity of the Pt/Sn/Rh ternary alloy–SnO_2 to the Pt/Rh binary alloy–SnO_2 reported here suggests that alloying between Pt, Rh and Sn atoms might play an important role in ethanol oxidation. The Pt/Sn/Rh–SnO_2 has a more filled Pt 5d band and lower lying d band

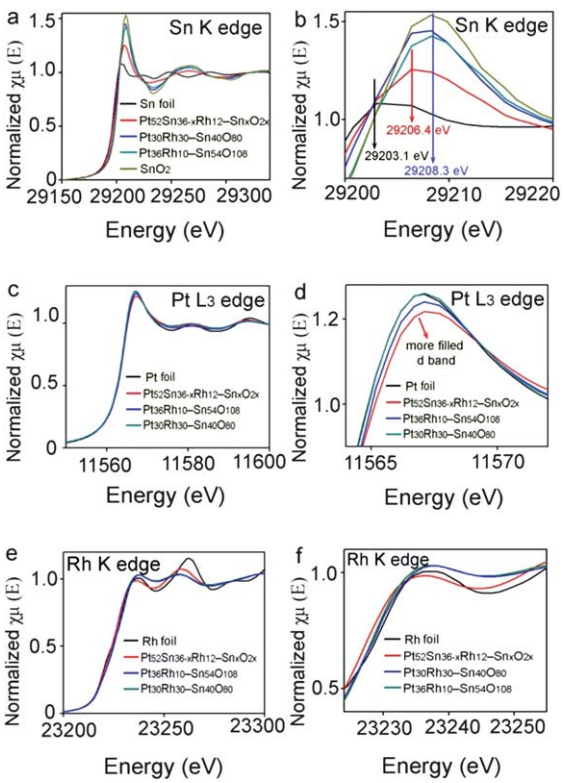

Fig. 4 (a and b) Sn K edge, (c and d) Pt L_3 edge and (e and f) Rh K edge normalized XANES spectra of $Pt_{52}Sn_{(36-x)}Rh_{12}$–$Sn_xO_{2x}$/C, $Pt_{36}Rh_{10}Sn_{54}$/C and $Pt_{30}Rh_{30}Sn_{40}$/C along with references.

center than the Pt/Rh–SnO_2, due to more Sn interactions with Pt and Rh as shown in Fig. 4. Thus, the Pt/Sn/Rh alloy, though less reactive for ethanol dissociative adsorption due to the lower d band center, might be, nonetheless, more active toward ethanol oxidation; Pt/Sn/Rh has a weaker bind to blocking intermediates making it more resistant to poisoning.[30,37] The promotional effects of a lower d band center on the activation of the O-containing intermediates have also been reported previously.[32,38,39]

Conclusions

Here we demonstrated the synthesis of Pt/Sn/Rh ternary electrocatalysts with controlled chemical compositions. By carefully analyzing the structures of various catalysts using the complementary characterization techniques including HRTEM, EDS and EXAFS, we were able to identify that Sn existed in two forms in the $Pt_{52}Rh_{12}Sn_{36}$ catalyst for the first time: one is in the metallic form as a PtRhSn homogenous alloy, the other is in the oxide form as the SnO_2. The coexistence of both metallic and ionic Sn was also confirmed by XANES spectra as shown in Fig. 4, where the Sn K edge spectrum in $Pt_{52}Rh_{12}Sn_{36}$ appeared as mixed electronic states of metallic and ionic Sn.

The reported $Pt_{52}Sn_{(36-x)}Rh_{12}$–$Sn_xO_{2x}$/C ternary alloy–$SnO_2$ catalysts showed much higher activity and long-term stability towards ethanol oxidation reaction. In particular, $Pt_{52}Sn_{(36-x)}Rh_{12}$–$Sn_xO_{2x}$/C showed a high mass current density and a much better stability compared to the commercial benchmark Pt/C catalyst (ETEK) in the 15 hours reaction, whereas Pt/C showed no activity after 13 hours reaction (Table 2). Although Rh metal is more expensive that Pt metal ($2375 *vs.* $1787 per ounce as of April 2011), the high activity and the good stability, as well as the relative low Rh content (molar ratio: 12%) will make $Pt_{52}Sn_{(36-x)}Rh_{12}$–$Sn_xO_{2x}$/C an excellent anode catalyst for direct ethanol fuel cell reactions. In the long run, designing a low-cost electrocatalyst with a facile preparation routine will be the ultimate goal for the ethanol fuel cell reactions. The results from the related research from PI's group will be presented later, and will not be the focus of the current paper.

Acknowledgements

This work is supported by the UNH (XT, WD, CAL) and DOE (AIF, DE-FG02-03ER15476; DS and LZ, DE-AC02-98CH10886). CAL thanks for the REAP and SURF summer supports from UNH. The use of the NSLS was supported by the U.S. Department of Energy, Office of Science, Office of Basic Energy Sciences, under Contract No. DE-AC02-98CH10886. Beam lines X19A/X18B are partly supported by Synchrotron Catalysis Consortium (DE-FG02-05ER15688).

Reference

1 E. Antolini, *J. Power Sources*, 2007, **170**(1), 1–12.
2 G. A. Camara and T. Iwasita, *J. Electroanal. Chem.*, 2005, **578**(2), 315–321.
3 E. Casado-Rivera, D. J. Volpe, L. Alden, C. Lind, C. Downie, T. Vazquez-Alvarez, A. C. D. Angelo, F. J. DiSalvo and H. D. Abruna, *J. Am. Chem. Soc.*, 2004, **126**(12), 4043–4049.
4 H. S. Wang, L. Alden, F. J. DiSalvo and H. D. Abruna, *Phys. Chem. Chem. Phys.*, 2008, **10**(25), 3739–3751.
5 C. Lamy, S. Rousseau, E. M. Belgsir, C. Coutanceau and J. M. Leger, *Electrochim. Acta*, 2004, **49**(22–23), 3901–3908.
6 H. Wang, Z. Jusys and R. J. Behm, *J. Power Sources*, 2006, **154**(2), 351–359.
7 X. H. Xia, H. D. Liess and T. Iwasita, *J. Electroanal. Chem.*, 1997, **437** (1–2), 233–240.
8 W. X. Du, Q. Wang, D. Su, A. I. Frenkel and X. W. Teng, *Cryst. Growth Des.*, 2011, **11**(2), 594–599.
9 Y. W. Chang, C. W. Liu, Y. C. Wei and K. W. Wang, *Electrochem. Commun.*, 2009, **11**(11), 2161–2164.
10 A. Kowal, S. L. Gojkovic, K. S. Lee, P. Olszewski and Y. E. Sung, *Electrochem. Commun.*, 2009, **11**(4), 724–727.
11 A. Kowal, M. Li, M. Shao, K. Sasaki, M. B. Vukmirovic, J. Zhang, N. S. Marinkovic, P. Liu, A. I. Frenkel and R. R. Adzic, *Nat. Mater.*, 2009, **8**(4), 325–330.
12 M. Li, A. Kowal, K. Sasaki, N. Marinkovic, D. Su, E. Korach, P. Liu and R. R. Adzic, *Electrochim. Acta*, 2010, **55**(14), 4331–4338.
13 E. V. Spinace, R. R. Dias, M. Brandalise, M. Linardi and A. O. Neto, *Ionics*, 2010, **16**(1), 91–95.
14 Q. Yuan, Z. Y. Zhou, J. Zhuang and X. Wang, *Chem. Mater.*, 2010, **22**(7), 2395–2402.
15 E. Antolini, F. Colmati and E. R. Gonzalez, *J. Power Sources*, 2009, **193**(2), 555–561.
16 C. L. Cleveland, W. D. Luedtke and U. Landman, *Phys. Rev. Lett.*, 1998, **81**(10), 2036–2039.
17 Z. L. Wang, J. M. Petroski, T. C. Green and M. A. El-Sayed, *J. Phys. Chem. B*, 1998, **102**(32), 6145–6151.
18 S. Link, C. Burda, M. B. Mohamed, B. Nikoobakht and M. A. El-Sayed, *J. Phys. Chem. A*, 1999, **103**(9), 1165–1170.
19 A. Frenkel, *Z. Kristallogr.*, 2007, **222**(11), 605–611.
20 X. W. Teng, M. Feygenson, Q. Wang, J. Q. He, W. X. Du, A. I. Frenkel, W. Q. Han and M. Aronson, *Nano Lett.*, 2009, **9**(9), 3177–3184.
21 X. W. Teng, Q. Wang, P. Liu, W. Han, A. Frenkel, W. Wen, N. Marinkovic, J. C. Hanson and J. A. Rodriguez, *J. Am. Chem. Soc.*, 2008, **130**(3), 1093–1101.
22 D. R. Blasini, D. Rochefort, E. Fachini, L. R. Alden, F. J. DiSalvo, C. R. Cabrera and H. D. Abruna, *Surf. Sci.*, 2006, **600**(13), 2670–2680.
23 F. Colmati, E. Antolini and E. R. Gonzalez, *J. Alloys Compd.*, 2008, **456**(1–2), 264–270.
24 D. R. M. Godoi, J. Perez and H. M. Villullas, *J. Power Sources*, 2010, **195**(11), 3394–3401.
25 D. Grandjean, R. E. Benfield, C. Nayral, L. Erades, K. Soulantica, A. Maisonnat and B. Chaudret, *Phys. Scr.*, 2005, **115**, 699–702.
26 M. Tromp, J. A. van Bokhoven, G. P. F. van Strijdonck, P. van Leeuwen, D. C. Koningsberger and D. E. Ramaker, *J. Am. Chem. Soc.*, 2005, **127**(2), 777–789.
27 J. Greeley and M. Mavrikakis, *Nat. Mater.*, 2004, **3**(11), 810–815.
28 B. Lim, M. Jiang, P. H. C. Camargo, E. C. Cho, J. Tao, X. Lu, Y. Zhu and Y. Xia, *Science*, 2009, **324**, 1302–1305.
29 S. Maksimuk, S. C. Yang, Z. M. Peng and H. Yang, *J. Am. Chem. Soc.*, 2007, **129**(28), 8684–8685.
30 A. U. Nilekar, Y. Xu, J. L. Zhang, M. B. Vukmirovic, K. Sasaki, R. R. Adzic and M. Mavrikakis, *Top. Catal.*, 2007, **46**(3–4), 276–284.
31 Z. M. Peng and H. Yang, *J. Am. Chem. Soc.*, 2009, **131**(22), 7542–7543.
32 P. Strasser, S. Koh, T. Anniyev, J. Greeley, K. More, C. F. Yu, Z. C. Liu, S. Kaya, D. Nordlund, H. Ogasawara, M. F. Toney and A. Nilsson, *Nat. Chem.*, 2010, **2**(6), 454–460.
33 L. L. Wang and D. D. Johnson, *J. Phys. Chem. C*, 2008, **112**(22), 8266–8275.
34 D. Xu, Z. Liu, H. Yang, Q. Liu, J. Zhang, J. Fang, S. Zou and K. Sun, *Angew. Chem., Int. Ed.*, 2009, **48**, 1–6.
35 D. F. Yancey, E. V. Carino and R. M. Crooks, *J. Am. Chem. Soc.*, 2010, **132**(32), 10988–10989.
36 H. C. Ye and R. M. Crooks, *J. Am. Chem. Soc.*, 2007, **129**(12), 3627–3633.
37 J. Zhang, K. Sasaki, E. Sutter and R. R. Adzic, *Science*, 2007, **315** (5809), 220–222.
38 Y. Xu, A. V. Ruban and M. Mavrikakis, *J. Am. Chem. Soc.*, 2004, **126** (14), 4717–4725.
39 J. L. Zhang, M. B. Vukmirovic, Y. Xu, M. Mavrikakis and R. R. Adzic, *Angew. Chem., Int. Ed.*, 2005, **44**(14), 2132–2135.

